This is a peer-reviewed, accepted author manuscript of the following research article: Huang, C., Chen, K., Huang, M., Kong, D., & Yuan, J. (2024). Topology-preserving image registration with novel multi-dimensional Beltrami regularization. Applied Mathematical Modelling, 125(Part B), 539-556. https://doi.org/10.1016/j.apm.2023.09.033

Topology-Preserving Image Registration With Novel Multi-Dimensional Beltrami Regularization

Chongfei Huang[a,1], Ke Chen[b,1], Meixiang Huang[c], Dexing Kong[a], Jing Yuan[d,*]

a School of Mathematical Sciences, Zhejiang University, No.38 Zheda Road, Xihu District, Hangzhou, 310007, Zhejiang, China
b Dept of Mathematics and Statistics, University of Strathclyde, 26 Richmond Street, Glasgow G1 1XH, United Kingdom and Centre for Mathematical Imaging Techniques and Department of Mathematical Sciences, University of Liverpool, Liverpool L69 7ZL, Liverpool, United Kingdom *c School of Mathematics and Statistics, Minnan Normal University, No.36 Xianqian Street, Zhangzhou, 363000, Fujian, China*
d College of Mathematical Medicine, Zhejiang Normal University, No. 688 Yingbin Road, Jinhua, 321004, Zhejiang, China

Abstract

Beltrami coefficient provides a proper measure to quantify local distortions for a topology-preserving mapping, a.k.a general quasi-conformal mapping, in 2D. Recent studies managed to extend Beltrami coefficient from 2D to nD, and introduced its corresponding Beltrami-like measures to encode local deformation information in challenging nD topology-preserving image registration tasks. However, all these nD measures are not consistent with the classical 2D Beltrami coefficient. We propose a novel nD measure for evaluating local distortions of an nD diffeomorphic mapping in this work. We show its key mathematical properties, and prove that the new measure coincides with the classical 2D Beltrami coefficient. We further introduce a new nD topology-preserving image registration model by means of regularizing such proposed Beltrami-consistent coefficient, and show the existence of its solution. Meanwhile, a generalized Gauss-Newton scheme is applied to establish a fast multi-level numerical solver. Extensive experiments over different 3D medical image registration tasks, including the challenging multi-modal medical image registration, illustrate that the proposed approach by regu-

*Corresponding author, please contact Jing Yuan for more information.
Email address: `jyuan@zjnu.edu.cn` (Jing Yuan)
[1]Ke Chen shares equal contribution with Chongfei Huang.

larizing the introduced Beltrami-consistent coefficient outperforms the other state-of-the-art topology-preserving methods in both efficiency and accuracy.

Keywords: Topology-preserving, nD Beltrami coefficient, variational model, 3D image registration, Beltrami regularization

---

1. Introduction

Nonlinear (or non-rigid) image registration aims to discover an optimal mapping with locally varying deformations between different image acquisitions. It plays the fundamental role in many applications of image processing, particularly modern medical image analysis (see [1] and [2] for more references). In particular, for non-rigid medical image registration, finding the potential smooth and bijective, a.k.a. topology-preserving, mapping between two given images, which might come from different image modalities, is appreciated due to widely existing non-rigidity of human body and tissue. A large number of methods were proposed for non-rigid medical image registration from different optimization perspectives [3–6]; however, it still remains one of the most challenging tasks in practice, especially for registration incorporating topology-preserving priors. Even a proper mathematical description of anatomical deformation and matching criteria is fairly open, while incorrect models are usually the main reason to generate wrong results of image correspondence (even though visualisation may appear acceptable). To this end, diffeomorphism brings the most appropriate model of smooth and bijective, i.e. topology-preserving, mappings in theory [6–8]; either guaranteeing a continuous one-to-one invertible mapping or enforcing a positive Jacobian determinant of the result differentiable transformation, in practice, becomes two main ways to resolve such a topology-preserving mapping numerically.

Given the fixed template image $T : \Omega \subset \mathbb{R}^n \to \mathbb{R}$ and the moving image $M : \Omega \subset \mathbb{R}^n \to \mathbb{R}$, where Ω is some image domain in $\mathbb{R}^n$, the variational model to register the moving image M to the template image T by some transformation field $\mathbf{y}(\mathbf{x}) : \Omega \subset \mathbb{R}^n \to \mathbb{R}^n$ can be properly generalized as below:

$$\min_{\mathbf{y}} \; L(\mathbf{y}) := S(M \circ \mathbf{y}, T) + \alpha R(\mathbf{y}) \tag{1}$$

where $S(\cdot)$ is some fidelity measure evaluating the difference between the deformed moving image $M \circ \mathbf{y} := M(\mathbf{y}(\mathbf{x}))$ and the fixed template image T, and the regularization term $R(\mathbf{y})$ enforces the optimized transformation field

$\mathbf{y}(\mathbf{x})$ to meet some specified constraints, such as smoothness or topology-preservation.

In essence, the fidelity term $S(M \circ \mathbf{y}, T)$ of (1) is usually defined depending on the modalities of the template image T and moving image M: when both images of $T(\mathbf{x})$ and $M(\mathbf{x})$ share the same image modality, i.e. the corresponding pixels of both images have similar intensity values, some functions to directly penalize intensity differences between the images $M \circ \mathbf{y}$ and T are taken as the fidelity measure $S(M \circ \mathbf{y}, T)$, such as the most widely used sum of squared differences (SSD):

$$S(M \circ \mathbf{y}, T) = \frac{1}{2}\|M \circ \mathbf{y} - T\|^2 \ := \frac{1}{2}\int_{\Omega}(M(\mathbf{y}(\mathbf{x})) - T(\mathbf{x}))^2 d\mathbf{x}\,. \tag{2}$$

When both images of $T(\mathbf{x})$ and $M(\mathbf{x})$ have different image modalities, i.e. totally different image appearances, some complex fidelity measures $S(M \circ \mathbf{y}, T)$ are defined to evaluate complicated similarities between the two images $M \circ \mathbf{y}$ and T, such as normalized cross correlation (NCC), mutual information (MI) and comparing normalized gradient fields of $M \circ \mathbf{y}$ and T [9, 10] etc. On the other hand, the regularization function $R(\mathbf{y})$ of (1) encodes additional prior information on the transformation $\mathbf{y}$ to make the proposed optimization model (1) well-posed in mathematics. Many works were contributed to propose the regularization functions of $R(\mathbf{y})$ upon different transformation priors, such as the regularization of elasticity [11], the viscosity-based regularization [12], the regularization of smoothness [13, 14], the regularization based on various curvature definitions [15, 16], the fractional-order total-variation regularization [17], also the regularization based highly nontrivial topology-preservation which explicitly imposes the Jacobian determinant of $\mathbf{y}$ to be positive [8, 17], i.e. $\det \nabla\mathbf{y} > 0$.

Recent studies [18–20] show that the theory of quasi-conformal mapping provides a descent description of topology-preserving mappings. Especially, the extension of Beltrami coefficient $\mu(\mathbf{y})$, a key measure of local conformal distortion of 2D quasi-conformal mapping, from 2D to nD provides a very effective measure to encode the local dilation or shrinkage of a topology-preserving transformation $\mathbf{y}(\mathbf{x})$ in nD. In addition, we have $\mu(\mathbf{y}(\mathbf{x})) < 1 \Leftrightarrow \det \nabla\mathbf{y}(\mathbf{x}) > 0$. This means that the hard constraint of the challenging topology-preservation condition, i.e. $\det \nabla\mathbf{y}(\mathbf{x}) > 0$, can be implicitly kept by imposing $\mu(\mathbf{y}(\mathbf{x})) < 1$, which is much easier to implement in numerics. Actually, by registering two images, one image can be segmented from the other image by regions of user-prescribed topology, which is also known as atlas-based image segmentation in medical image analysis. To this end, topology-preserving image registration leads to the interesting application of topology-preserving image segmentation [21, 22], where Beltrami coefficient is utilized to keep topology of segmentation shapes such that detailed descriptions of shape prior and convexity are not necessary. However, all the proposed extensions of 2D Beltrami coefficient to nD space fail to be the original Beltrami coefficient when $n = 2$, i.e. not consistent with the classical Beltrami coefficient in 2D. A natural extension of the original 2D Beltrami coefficient to nD space is still missed, especially its essential mathematical properties and associate application to topology-preserving image registration.

Contributions: In this paper, we extend the famous Beltrami coefficient from 2D to nD, which is still missed in literature, and propose a novel nD Beltrami-coefficient-based measure for evaluating local distortion of a diffeomorphic mapping. We further prove its key properties in mathematics and show its close relationship with the topology-preserving constraint of a diffeomorphic mapping $\mathbf{y}$, i.e. the Jacobian determinant of the mapping $\mathbf{y}$ should be positive such that $\det\nabla\mathbf{y} > 0$. In addition, we introduce a new image registration model based on regularizing the novel nD Beltrami-consistent coefficient and demonstrate the existence of its solution. We further utilize a generalized Gauss-Newton scheme to solve the proposed non-rigid registration model efficiently. Extensive experiments over different image registration tasks in 3D, including the challenging multi-modal medical image registration, illustrate that the proposed Beltrami-consistent coefficient-based registration model outperforms the other state-of-the-art topology-preserving methods in both efficiency and accuracy.

Organization and Notations: The rest of the paper is organized as follows. In section 2, we briefly review related works. In section 3, we propose our new registration model for 3D image registration and illustrate the existence of the solution and numerical implementation. Numerical experimental results are shown in section 4, and finally, a conclusion is summarized in section 5.

In this work, let $\mathbf{f}(x_1, ..., x_n) = \big(f_1(x_1, ..., x_n), ..., f_n(x_1, ..., x_n)\big)$ denote the nD transformation field, $\nabla\mathbf{f}$ its associate $n \times n$ Jacobian matrix and $\det(\nabla\mathbf{f})$ the determinant of its Jacobian matrix. Likely, in 3D, we denote $\mathbf{y}(\mathbf{x}) = (y_1(\mathbf{x}), y_2(\mathbf{x}), y_3(\mathbf{x}))$ as the transformation at some position $\mathbf{x} = (x_1, x_2, x_3)$ in some 3D image domain Ω, and $\det(\nabla\mathbf{y})$ gives the determinant of its associate Jacobian matrix $\nabla\mathbf{y}$.

2. Previous Studies

Topology-preserving image registration is essentially looking for an optimal smooth and bijective mapping between images. It is of great interest in many applications, particularly in medical image registration, where elasticity of a human body determines the transformation between different images of the same body is naturally smooth and bijective. Registration include the hyperelastic model (Hyper) [7] by enforcing the Jacobian determinant of the mapping $\mathbf{y}$ close to 1 for preserving topology at each pixel, and the large deformation differential metric mapping model (LDDMM) [6, 23] which extracts the optimal diffeomorphic transformation between two images by solving a smooth time-varying flow PDE. Lars Ruthotto [24] systematically explained the theory of the hyperelastic model with numerical practices in his PhD thesis and Zhang et al [25] used the hyperelastic constraint technique for image segmentation. Given that such hyperelastic-based regularization term actually imposes the Jacobian determinant of a mapping $\mathbf{y}$ tends to be 1 locally, it often generates an over-smooth hence inaccurate mapping in practice. On the other hand, provided the fact that evolving a mapping, while still preserving topology, over time leads to a big load in both computation and memory, LDDMM-based methods including most recent developments [8, 26] result in high numerical cost but low computational efficiency. In Sec. 4, we will further show the disadvantages of both two classical approaches in our experiments for comparison.

Recently, the theory of quasi-conformal mapping was introduced as a powerful mathematical model to describe such physically topology-preserving mappings for image registration. Moreover, the latest studies aimed to extend the well-known Beltrami coefficient, a key quantity to evaluate conformality distortion of a 2D quasi-conformal mapping, from 2D to nD and build up its related regularization functions in the corresponding variational image registration models. In this section, we review two representative works of LLL model (Lee, Lam, and Lui [20]) and ZC model (Zhang and Chen [19]).

2.1. nD Quasi-Conformal Mappings – LLL model

Intuitively, a quasi-conformal mapping, a.k.a. a general diffeomorphism, maps infinitesimal circles on one domain to the infinitesimal ellipses on the range domain, which stands for an orientation-preserving homeomorphism with bounded conformality distortion. In 2D, a quasi-conformal map $f(z)$: $\mathrm{C} \rightarrow \mathrm{C}$, where C denotes the space of complex values (2D vectors), satisfies the classical Beltrami equation

$$\frac{\partial f}{\partial \tilde{z}} = \mu(z) \frac{\partial f}{\partial z}\,, \tag{3}$$

for some complex valued measure $\mu(z)$, called Beltrami coefficient, along with $\|\mu\|_\infty \leq 1$. The map f is conformal locally when its Beltrami coefficient vanishes $\mu(z) = 0$, but non-conformal otherwise; in another words, the Beltrami coefficient $\mu(z)$ evaluates local non-conformality, i.e. the eccentricity and orientation of a local infinitesimal ellipse.

In view of the above Beltrami equation (3), the complex value $\tilde{z}$ is just perpendicular to z in the complex space C which can be equally viewed as a 2D vector space. The Beltrami coefficient $\mu(z)$ in (3) determines not only the angle between the two directions of maximal magnification and maximal shrinkage, which are $\arg(\mu)/2$ and $(\arg(\mu) - \pi)/2$, but also the amount of magnification factor and shrinkage factor, which are $1 + |\mu|$ and $1 - |\mu|$ respectively. Thus, the local dilation can be computed by

$$K_d(f) := \frac{1 + |\mu|}{1 - |\mu|}\,, \tag{4}$$

which essentially quantifies the distortion of an infinitesimal ball to an infinitesimal ellipsoid under a quasi-conformal mapping. On the other hand, it is easy to observe that the maximal magnification factor and the maximal shrinkage factor of a 2D mapping f are just given by the maximum and minimum of two eigenvalues of $\nabla f^T \nabla f$ respectively, and the mapping f becomes conformal, i.e. $K_d(f) = 1$, only when the two eigenvalues of the matrix $\nabla f^T \nabla f$ are equal. This exactly inspired extending such a quasi-conformality measure K_d from 2D space to nD space.

Let $\mathbf{f}$ be an nD quasi-conformal mapping and $\lambda_1, ..., \lambda_n$ be the eigenvalues of the matrix $\nabla \mathbf{f}^T \nabla \mathbf{f}$. We then have

$$\|\nabla \mathbf{f}\|_F^2 \;=\; \mathrm{Tr}(\nabla \mathbf{f}^T \nabla \mathbf{f}) \;=\; \lambda_1 + \cdots + \lambda_n\,, \quad (\det \nabla \mathbf{f})^2 \;=\; \det(\nabla \mathbf{f}^T \nabla \mathbf{f}) \;=\; \lambda_1 \cdots \lambda_n\,.$$

It is well-known that

$$(\lambda_1 \cdots \lambda_n)^{1/n} \;\leq\; (\lambda_1 + \cdots + \lambda_n)/n\,, \tag{5}$$

i.e. the arithmetic mean of $\lambda_1, ..., \lambda_n$ is not less than their geometric mean, where the equality holds only when all the eigenvalues $\lambda_1, ..., \lambda_n$ are equal.

Observe this, LLL model proposed the local distortion measure of one nD mapping $\mathbf{f}$ by the ratio of its arithmetic mean and geometric mean of the eigenvalues of $\nabla\mathbf{f}^T\nabla\mathbf{f}$ such that

$$K(\mathbf{f}) = \begin{cases} \dfrac{1}{n}\dfrac{\|\nabla\mathbf{f}\|_F^2}{(\det\nabla\mathbf{f})^{2/n}} & \text{if } \det\nabla\mathbf{f} > 0 \\ +\infty & \text{otherwise} \end{cases} . \tag{6}$$

Clearly, in view of (5), such conformality distortion measurement $K(\mathbf{f})$ of a quasi-conformal mapping $\mathbf{f}$ is not less than 1, i.e. $K(\mathbf{f}) \geq 1$, and the mapping $\mathbf{f}$ becomes conformal when $K(\mathbf{f}) = 1$ such that all the eigenvalues of $\nabla\mathbf{f}^T\nabla\mathbf{f}$ are equal. So the value of $K(\mathbf{f})$ properly measures the distance of $\mathbf{f}$ from a conformal mapping.

They further introduced the minimization of K as a new regularization term in the 3D landmark-based registration model (LLL model):

$$\min_{\mathbf{y}} \frac{\|\nabla\mathbf{y}\|_F^2}{3(\det\nabla\mathbf{y})^{2/3}} + \frac{\alpha}{2}\|\Delta\mathbf{y}\|_2^2 \qquad \text{s.t. } \det\mathbf{y} > 0, \text{ and } \mathbf{y}(p_i) = q_i,\ i = 1, \ldots, m \tag{7}$$

where $\mathbf{y}(\mathbf{x})$ is a mapping in 3D and p_i and q_i are the corresponding landmark points. In addition, an ADMM-based algorithm was proposed to solve the highly nonlinear optimization problem (7) by tackling its two key subproblems alternately, while keeping the challenging hard constraint $\det\mathbf{y} > 0$ carefully at each step.

2.2. Beltrami Coefficient-Like Regularization – [19]

Given the relationship between the Beltrami coefficient μ and its distortion measure K by (4), we have

$$|\mu| = \frac{K-1}{K+1} . \tag{8}$$

It is easy to see that there is a one-to-one mapping between $|\mu|$ and K for any $K \geq 1$, and $\mu = 0$ while $K(\mathbf{f}) = 1$ and the mapping $\mathbf{f}$ becomes conformal. This means that both $|\mu|$ and K can be used to quantify local distortions of a quasi-conformal mapping in nD. Follow this idea, the Beltrami coefficient-like measure $N_1(\mathbf{y})$ (ZCO1) for regularizing a 3D mapping $\mathbf{y}$ is proposed by [19] such that

$$N_1(\mathbf{y}) = \frac{\|\nabla\mathbf{y}\|_F^2 - 3(\det\nabla\mathbf{y})^{2/3}}{\|\nabla\mathbf{y}\|_F^2 + 3(\det\nabla\mathbf{y})^{2/3}}, \tag{9}$$

which just mimics $|\mu|$ in (8) given $K(\mathbf{y})$ as (6). Also, another measure $N_2(\mathbf{y}) = K(\mathbf{y})$ (ZCO2) as (6) for comparisons, i.e.

$$N_2(\mathbf{y}) = K(\mathbf{y}) = \frac{1}{3}\frac{\|\nabla \mathbf{y}\|_F^2}{(\det \nabla \mathbf{y})^{2/3}}. \tag{10}$$

However, both (9) and (10) cannot obtain the required topology-preserving transformation by controlling their values, hence the associate hard constraint $\det \nabla \mathbf{y} > 0$ must be kept explicitly at each step. To this end, [19] proposed **another** Beltrami coefficient-like quantity $N(\mathbf{y})$ w.r.t. the 3D continuously differentiable mapping $\mathbf{y}(\mathbf{x})$ such that

$$N(\mathbf{y}) = \frac{\|\nabla \mathbf{y}\|_F - \sqrt{3}(\det \nabla \mathbf{y})^{1/3}}{\|\nabla \mathbf{y}\|_F + \sqrt{3}(\det \nabla \mathbf{y})^{1/3}} \tag{11}$$

as a local conformality distortion measure of $\mathbf{y}$, and proved its key mathematical property

$$N(\mathbf{y}) < 1 \iff \det \nabla \mathbf{y} > 0\,, \tag{12}$$

which is similar as the 2D Beltrami coefficient.

Accordingly, one only needs to enforce the constraint $N(\mathbf{y}) < 1$ implicitly, instead of keeping $\det \nabla \mathbf{y} > 0$ explicitly. The following ZC model of 3D topology-preserving image registration is hence proposed:

$$\begin{aligned}\min_{\mathbf{y}} J(\mathbf{y}) := D(M \circ \mathbf{y}, T) + \frac{\alpha_1}{2}\int_\Omega \|\nabla(\mathbf{y}-\mathbf{x})\|_F^2 dx \\ + \frac{\alpha_2}{2}\int_\Omega \|\nabla^2(\mathbf{y}-\mathbf{x})\|_F^2 dx + \beta \int_\Omega \Phi(N(\mathbf{y}))dx\end{aligned} \tag{13}$$

where the first term of data fidelity evaluates the disparity between the template image T and the moving image $M \circ \mathbf{y}$, the second and third term impose the smoothness of transformation, the penalty function $\Phi(v) = v^2/[(v-1)^2+1]$ in the fourth term enforces $N(\mathbf{y}) < 1$, i.e. $\det \nabla \mathbf{y} > 0$ for a topology-preserving mapping.

The 3D conformality distortion measure (11) can be also generalized for one nD quasi-conformal mapping $\mathbf{f}$ as below :

$$N(\mathbf{f}) = \begin{cases} \dfrac{\|\nabla \mathbf{f}\|_F - \sqrt{n}(\det \nabla \mathbf{f})^{\frac{1}{n}}}{\|\nabla \mathbf{f}\|_F + \sqrt{n}(\det \nabla \mathbf{f})^{\frac{1}{n}}} & \text{if n is odd} \\ \dfrac{\|\nabla \mathbf{f}\|_F - \sqrt{n}(\det \nabla \mathbf{f})^{\frac{1}{n}}}{\|\nabla \mathbf{f}\|_F + \sqrt{n}(\det \nabla \mathbf{f})^{\frac{1}{n}}} & \text{if n is even and } \det \nabla \mathbf{f} > 0 \\ \infty & \text{otherwise} \end{cases} \tag{14}$$

However, such extension (14) has a complex form due to the parity of n, since $\det \nabla \mathbf{y} > 0$ is required for the even n. Meanwhile, the new measure given in (14) does not coincide with the classical 2D Beltrami coefficient $|\mu|$ when $n = 2$. Actually, for 2D and $\det \nabla \mathbf{y} > 0$, the classical 2D Beltrami coefficient $|\mu|$ satisfies

$$|\mu|^2 = \frac{\|\nabla \mathbf{y}\|_F^2 - 2\det \nabla \mathbf{y}}{\|\nabla \mathbf{y}\|_F^2 + 2\det \nabla \mathbf{y}}\,, \tag{15}$$

which holds the following inequality:

$$N(\mathbf{y}) \le |\mu(\mathbf{y})|^2 \le 2N(\mathbf{y})\,, \quad \text{i.e. } |\mu(\mathbf{y})|^2 \iff N(\mathbf{y})\,. \tag{16}$$

We see that the measure $N(\mathbf{y})$ proposed in [19] is closely related to the standard Beltrami coefficient $\mu(\mathbf{y})$ in 2D, but they are not the same. In another word, the generalized nD Beltrami coefficient-like measure $N(\mathbf{f})$ given in (14) does not results in the original 2D Beltrami coefficient μ while $n = 2$, i.e. not consistent with the original 2D Beltrami coefficient μ. In this work, we will improve this conformality distortion measure by directly extending from the 2D Beltrami coefficient and show its advantages in both theory and numerical practices of topology-preserving image registration.

3. Beltrami-Consistent Coefficient and Image Registration

In this section, we first propose a novel nD Beltrami coefficient which coincides with the original Beltrami coefficient (15) in 2D, i.e. it is indeed consistent with the 2D Beltrami coefficient and can be viewed as its natural extension in nD. We demonstrate its key mathematical properties which ensure that the introduced Beltrami-consistent coefficient can act as a proper measure to impose the local conformality of a diffeomorphic mapping. Based upon it, we introduce the new variational topology-preserving image registration model and prove the existence of its solution. We finally present a detailed numerical algorithm for solving the proposed model efficiently.

3.1. Beltrami Coefficient-Consistent Measure in nD

Now we define the new conformality measure of one nD map as follows

Definition 3.1. *Given the nD map* $\mathbf{f}$ *which is continuously differentiable, then its Beltrami coefficient-consistent measure of conformality is defined as:*

$$N(\mathbf{f}) = \frac{\|\nabla \mathbf{f}\|_F^2 - n\,\mathrm{sign}(\det \nabla \mathbf{f})(\det \nabla \mathbf{f})^{2/n}}{\|\nabla \mathbf{f}\|_F^2 + n\,\mathrm{sign}(\det \nabla \mathbf{f})(\det \nabla \mathbf{f})^{2/n}}\,. \tag{17}$$

In contrast with the Beltrami coefficient-like measure (14) proposed in [19], the new conformality measure (17) enjoys two great advantages: first, it does not need considering the parity of n since the sign of $\det \nabla \mathbf{f}$ is built-in; second, for the 2D case ($n = 2$), the new measure (17) boils down to the standard Beltrami coefficient $|\mu|$ (15) with precisely $N(\mathbf{f}) = |\mu|^2$, which is consistent with the definition of 2D Beltrami coefficient.

In addition, the proposed new measure also shares the same key properties with the Beltrami coefficient-like measure (14) and can be used as an appropriate criterion to measure the distance from conformal maps. We list and prove such important properties in the following part:

Lemma 3.2. *The quantity $N(\mathbf{f})$ defined by (17) for an nD map $\mathbf{f}$ possesses the following properties when $\nabla \mathbf{f}$ is non-degenerated such that $\|\nabla \mathbf{f}\|_F \neq 0$:*

- P_1 *$N(\mathbf{f})$ is non-negative, i.e. $N(\mathbf{f}) \geq 0$.*
- P_2 $N(\mathbf{f}) < 1 \iff \det \nabla \mathbf{f} > 0$.
- P_3 $N(\mathbf{f}) = 1 \iff \det \nabla \mathbf{f} = 0$.
- P_4 $N(\mathbf{f}) > 1 \iff \det \nabla \mathbf{f} < 0$.
- P_5 *If all the singular values of the matrix $\nabla \mathbf{f}$ are equal, then $N(\mathbf{f}) = 0$ when $\det \nabla \mathbf{f} > 0$, and $N(\mathbf{f})$ becomes ∞ when $\det \nabla \mathbf{f} < 0$. Specially, if $N(\mathbf{f}) = 0$, then all the eigenvalues of $(\nabla \mathbf{f})^T \nabla \mathbf{f}$ are equal.*
- P_6 *$N(\mathbf{f})$ is invariant under the scalar multiplication and rigid-body motion actions.*

Proof. Let σ_1, σ_2, $\cdots$, and σ_n be the singular values of $\nabla \mathbf{f}$, then we have

$$\|\nabla \mathbf{f}\|_F^2 = \sum_{i=1}^{n} \sigma_i^2 = \sum_{i=1}^{n} \lambda_i \geq 0\,, \qquad (\det \nabla \mathbf{f})^2 = \prod_{i=1}^{n} \sigma_i^2 = \prod_{i=1}^{n} \lambda_i \geq 0\,, \quad (18)$$

where $\lambda_i = \sigma_i^2$, $i = 1 \cdots n$, be the eigenvalues of the matrix $(\nabla \mathbf{f})^T \nabla \mathbf{f}$. Since $\nabla \mathbf{f}$ is non-degenerated, i.e. $\|\nabla \mathbf{f}\|_F \neq 0$, the n eigenvalues λ_1 ... λ_n are hence not all zeros and $\|\nabla \mathbf{f}\|_F^2 > 0$. Note: The proofs below follow this fact in default.

Then, in view of (5), it is easy to see that both denominator and numerator of $N(\mathbf{f})$ in (17) are non-negative. P_1 is hence proved such that $N(\mathbf{f})$ is non-negative.

For P_2, given $N(\mathbf{f}) < 1$ and (17), we obtain

$$\|\nabla\mathbf{f}\|_F^2 - n\,\mathrm{sign}(\det\nabla\mathbf{f})(\det\nabla\mathbf{f})^{2/n} \;<\; \|\nabla\mathbf{f}\|_F^2 + n\,\mathrm{sign}(\det\nabla\mathbf{f})(\det\nabla\mathbf{f})^{2/n}\,,$$

and

$$\mathrm{sign}(\det\nabla\mathbf{f})(\det\nabla\mathbf{f})^{2/n} \;>\; 0\,.$$

Observing $(\det\nabla\mathbf{f})^{2/n} \geq 0$, we then have $\mathrm{sign}(\det\nabla\mathbf{f}) = 1$, i.e. $\det\nabla\mathbf{f}$ is positive.

On the other hand, if $\det\nabla\mathbf{f}$ is positive, then $\mathrm{sign}(\det\nabla\mathbf{f}) = 1$ and the definition $N(\mathbf{f})$ in (17) results in

$$N(\mathbf{f}) = \frac{\|\nabla\mathbf{f}\|_F^2 - n\,(\det\nabla\mathbf{f})^{2/n}}{\|\nabla\mathbf{f}\|_F^2 + n\,(\det\nabla\mathbf{f})^{2/n}} < 1\,.$$

P_2 is thus proved.

For P_3, if $N(y) = 1$, then, by (17), we have $\mathrm{sign}(\det\nabla\mathbf{f})(\det\nabla\mathbf{f})^{2/n} = 0$. Hence, $\det\nabla\mathbf{f} = 0$ is obtained.

In addition, if $\det\nabla\mathbf{f} = 0$, then $\mathrm{sign}(\det\nabla\mathbf{f}) = 0$. The denominator and numerator of $N(\mathbf{f})$ in (17) are both equal, we hence have $N(\mathbf{f}) = 1$. P_3 is proved accordingly.

For P_4, following similar steps as in the proof of P_2, it is easy to prove P_4.

For P_5, if all the singular values of the matrix $\nabla\mathbf{f}$ are equal, then the equality of (5) holds and we have

$$\|\nabla\mathbf{f}\|_F^2 \;=\; n\,(\det\nabla\mathbf{f})^{2/n}\,.$$

Clearly, either the denominator or numerator of $N(\mathbf{f})$ in (17) becomes zero depending on the sign of $\det\nabla\mathbf{f}$. So the first part of P_5 is proved.

Moreover, if $N(\mathbf{f}) = 0$, then the numerator of $N(\mathbf{f})$ in (17) vanishes. Given (5), this only holds when all the eigenvalues of the matrix $\nabla\mathbf{f}^T\nabla\mathbf{f}$ are equal. We then prove P_5.

For P_6, for the transformation $c\,\mathbf{f}$ where $c > 0$, $c\sigma_1, \cdots, c\sigma_n$ are the singular values of the matrix $\nabla c\,\mathbf{f}$. So we have

$$\|\nabla c\,\mathbf{f}\|_F^2 \;=\; c^2\sum_{i=1}^{n}\sigma_i^2\,, \qquad \det\nabla c\,\mathbf{f} \;=\; c^n\prod_{i=1}^{n}\sigma_i\,,$$

thus, in view of (17), $N(\mathbf{f}) = N(c\,\mathbf{f})$.

In addition, if O is an orthogonal matrix and $\mathbf{b}$ is a translation, then the Jacobian of $\mathbf{f}(O\mathbf{x}+\mathbf{b})$ is $O^T\nabla\mathbf{f}$. Since all the singular values of $\nabla\mathbf{f}$ and $O^T\nabla\mathbf{f}$ are the same, we then have $N(\mathbf{f}(\mathbf{x})) = N(\mathbf{f}(O\mathbf{x}+\mathbf{b}))$. Hence, the defined measure $N(\mathbf{f})$ in (17) is invariant under the scalar multiplication and rigid-body motion actions. Hence P_6 is proved. □

Note that the property P_2 in Lemma 3.2, i.e. $N(\mathbf{f}) < 1 \iff \det\nabla\mathbf{f} > 0$ in nD, is exactly consistent with the key property of the Beltrami coefficient in 2D. This is the main motivation to enforce $N(\mathbf{f}) < 1$ in the proposed image registration model, so as to obtain an optimal transformation with bijectivity and enough smoothness, see Sec. 3.2 for more details.

Also, as shown in [27], a general diffeomorphic transformation $\mathbf{f}$, i.e. $\det\nabla\mathbf{f} > 0$, is conformal if and only if:

$$\nabla\mathbf{f}^T\nabla\mathbf{f} = (\det\nabla\mathbf{f})^{2/n}\mathbf{I}\,, \tag{19}$$

where $\mathbf{I}$ is the identity matrix. We can then extend the second part of P_5 in Lemma 3.2 such that

Corollary 3.3. *For the nD map $\mathbf{f}$, if $N(\mathbf{f}) = 0$, then $\mathbf{f}$ is conformal.*

The proof simply follows the proof of the second part of P_5 in Lemma 3.2: if $N(\mathbf{f}) = 0$, the numerator of $N(\mathbf{f})$ in (17) becomes zero. It is easy to see that $\det\nabla\mathbf{f} > 0$ and all the eigenvalues of the matrix $\nabla\mathbf{f}^T\nabla\mathbf{f}$ are equal, then (19) clearly holds, which means that the nD map $\mathbf{f}$ is conformal.

Moreover, inspired by the definition of 2D distortion measurement K_d (4), we can similarly define the following generalized distortion measurement $K(f)$ in nD by Beltrami coefficient-consistent $N(\mathbf{f})$:

$$K_n(\mathbf{f}) = \frac{1+|\mu_n(\mathbf{f})|}{1-|\mu_n(\mathbf{f})|}\,, \quad \text{where } |\mu_n(\mathbf{f})|^2 = N(\mathbf{f})\,. \tag{20}$$

We consequently have an interesting result as follows:

Proposition 3.4. *For the nD map $\mathbf{f}$, $\mathbf{f}$ is conformal if and only if $K_n(\mathbf{f}) = 1$, i.e.*

$$\mathbf{f} \text{ is conformal} \iff K_n(\mathbf{f}) = 1\,.$$

Proof. First, if $\mathbf{f}$ is conformal, then (19) holds. By simple calculation, we have

$$\|\nabla \mathbf{f}\|_F^2 = n(\det \nabla \mathbf{f})^{\frac{2}{n}}.$$

Follow this and (20), it is easy to see that:

$$K_n(\mathbf{f}) + \frac{1}{K_n(\mathbf{f})} = \frac{2(1+|\mu_n(\mathbf{f})|^2)}{1-|\mu_n(\mathbf{f})|^2} = \frac{2}{n}\frac{\|\nabla \mathbf{f}\|_F^2}{(\det \nabla \mathbf{f})^{\frac{2}{n}}} = 2\,. \tag{21}$$

We thus obtain $K_n(\mathbf{f}) = 1$. The first part is proved.

On the other hand, if $K_n(\mathbf{f}) = 1$, then, in view of (20), it is obvious to see that $\mu_n(\mathbf{f}) = 0$, i.e. $N(\mathbf{f}) = \mu_n(\mathbf{f}) = 0$. By Coro. 3.3, the nD transformation $\mathbf{f}$ is conformal. The second part is proved. ☐

In addition, we also have

Proposition 3.5. *For the nD map* $\mathbf{f}$, $\det \nabla \mathbf{f} > 0$ *if and only if* $K_n(\mathbf{f}) \geq 1$, *i.e.*

$$\det \nabla \mathbf{f} > 0 \iff K_n(\mathbf{f}) \geq 1\,.$$

We apparently have $K_n(\mathbf{f}) \geq 1 \iff 0 \leq N(\mathbf{f}) < 1$. By P_1 and P_2 of Lemma 3.2, the proof is clear.

Particularly, we see that the nD transformation f turns to be conformal, i.e. $K_n(\mathbf{f}) \to 1$, when $N(\mathbf{f}) \to 0$; on the other hand, the nD distortion measurement $K_n(\mathbf{f})$ tends to be positive infinity, i.e. $K_n(\mathbf{f}) \to +\infty$ and the local distortion becomes extremely big, when $N(\mathbf{f}) \to 1^-$.

3.2. Beltrami-Consistent Image Registration

Both measures proposed in (17) and (20) can properly work as the distortion measurement of diffeomorphic transformations in nD. Especially, the introduced novel measure (17) is consistent with Beltrami coefficient in 2D, and is simpler than the other generalized distortion measure (20); hence, we propose and study the new image registration model in 3D based on the novel 3D Beltrami consistent measure (17):

$$\begin{aligned}\min_{\mathbf{y}} L(\mathbf{y}) := D(M \circ \mathbf{y}, T) &+ \frac{\alpha_1}{2}\int_\Omega ||\nabla(\mathbf{y}-\mathbf{x})||_F^2 d\mathbf{x} \\ &+ \frac{\alpha_2}{2}\int_\Omega ||\nabla^2(\mathbf{y}-\mathbf{x})||_F^2 d\mathbf{x} + \beta\int_\Omega \Phi(N(\mathbf{y}))d\mathbf{x}\end{aligned} \tag{22}$$

where the first data-fidelity term $D(M \circ \mathbf{y}, T)$ is to enforce image similarities between the template image T and moving image $M \circ \mathbf{y}$, the second and third terms regularize the smoothness of transformation $\mathbf{y}$, and the last term imposes the diffeomorphism condition $N(\mathbf{y}) < 1$, i.e. $\det \nabla \mathbf{y} > 0$, by minimizing $\Phi(v) = v^2/[(v-1)^2 + 1]$.

In this work, we also focus on the 3D non-rigid registration of two images from different image modalities, which is challenging in practice. In this context, we employ the data-fidelity term either by comparing normalized intensity gradients, i.e. directions of intensity gradient, of the two images $M \circ \mathbf{y}$ and T such that

$$D(M\circ\mathbf{y}, T) \;=\; \int_\Omega |\nabla^* M\circ\mathbf{y} - \nabla^* T|^2 dx + (|\nabla^* M\circ\mathbf{y}| + |\nabla^* T| - |\nabla^* M\circ\mathbf{y} + \nabla^* T|)^2 d\mathbf{x}\,, \tag{23}$$

where ∇^* denotes the normalized gradient operator, or based on the normalized cross correlation (NCC) of two image intensities as

$$\mathrm{NCC}(M\circ\mathbf{y}, T) = \frac{\int_\Omega \left((M\circ\mathbf{y})(\mathbf{x}) - \overline{(M\circ\mathbf{y})}\right)\left(T(\mathbf{x}) - \overline{T}\right) d\mathbf{x}}{\sqrt{\int_\Omega \left(M\circ\mathbf{y}(\mathbf{x}) - \overline{(M\circ\mathbf{y})}\right)^2 d\mathbf{x}}\sqrt{\int_\Omega \left(T(\mathbf{x}) - \overline{T}\right)^2 d\mathbf{x}}} \tag{24}$$

where $\overline{(M \circ \mathbf{y})}$ and $\overline{T}$ represent the respective intensity means of the deformed moving image $M \circ \mathbf{y}$ and template image T; for example, $D(M \circ \mathbf{y}, T) = -\mathrm{NCC}(M \circ \mathbf{y}, T)$ or $(1 - \mathrm{NCC}(M \circ \mathbf{y}, T)$ etc.

Additionally, for the sign function $\mathrm{sign}(\det \nabla \mathbf{f})$ in (17), which is discontinuous at zero point, we thus employ the following smooth function to approximate it instead:

$$\mathrm{sign}_\epsilon(t) = \frac{2}{\pi}\arctan(\frac{t}{\epsilon})\,, \tag{25}$$

where $\epsilon > 0$ is small.

We assume that, in this study, all the given images are continuously differentiable and compactly supported in Ω, and the transformations are second-order derivativable. Now we analyze the existence of the minimizer for the proposed optimization model (22) in the function space $W^{2,2}(\Omega)$.

Without loss of generality, we first list the following two facts [28]:

Definition 3.6. *Let $\Omega \subset \mathbb{R}^3$ be an open set. Assume $f : \Omega \times \mathbb{R}^3 \times \mathbb{R}^{3\times 3} \times \mathbb{R}^{3\times 3\times 3} \to [0, +\infty)$ satisfies the following conditions:*

(i) $f(\mathbf{x},\cdot,\cdot,\cdot)$ *is continuous for almost every* $x \in \Omega$
(ii) $f(\mathbf{x},\mathbf{y},\psi,\Theta)$ *is measurable in* $\mathbf{x}$ *for every* $(\mathbf{y},\psi,\Theta) \in \mathbb{R}^3 \times \mathbb{R}^{3\times 3} \times \mathbb{R}^{3\times 3\times 3}$.

Then f *is a Carathéodory function.*

Lemma 3.7. *Let* $\Omega \subset \mathbb{R}^3$ *be an open set. Assume* $f : \Omega \times \mathbb{R}^3 \times \mathbb{R}^{3\times 3} \times \mathbb{R}^{3\times 3\times 3} \to [0,+\infty)$ *satisfies the following conditions:*

(i) f *is a Carathéodory function.*
(ii) $f(\mathbf{x},\mathbf{y},\psi,\Theta)$ *is quasiconvex with respect to* Θ.
(iii) $0 \leq f(\mathbf{x},\mathbf{y},\psi,\Theta) \leq a(\mathbf{x})+C(|\mathbf{y}|^2+|\psi|^2+|\Theta|^2)$ *where* $a(\mathbf{x}) \in L^1(\Omega), C \geq 0$.

Then $L(\mathbf{y}) = \int_\Omega f(\mathbf{x},\mathbf{y},\psi,\Theta)dx$ *is weak lower semi-continuous (denoted by wlsc) in* $W^{2,2}(\Omega)$.

We can essentially rewrite the objective function (22) as below:

$$L(\mathbf{y}) = \int_\Omega f(\mathbf{x},\mathbf{y},\nabla\mathbf{y},\nabla^2\mathbf{y})dx\,, \tag{26}$$

where

$$\begin{aligned} f(\mathbf{x},\mathbf{y},\psi,\Theta) &= D(M\circ\mathbf{y},T) + \frac{\alpha_1}{2}|\psi - I|^2 + \frac{\alpha_2}{2}|\Theta|^2 \\ &+\beta\Phi\Big(\frac{\|\psi\|_F^2 - 3\,\mathrm{sign}_\epsilon(\det\psi)(\det\psi)^{2/3}}{\|\psi\|_F^2 + 3\,\mathrm{sign}_\epsilon(\det\psi)(\det\psi)^{2/3}}\Big) \end{aligned}$$

and $D(M\circ\mathbf{y},T)$ is given in (23).

The solution space is further defined as $W = \{y \in W^{2,2}(\Omega) : y(x) = x \text{ on } \partial\Omega\}$. Then, we have the following result.

Proposition 3.8. *If the template image* M *and the moving image* T *are continuously differentiable and compactly supported in* Ω, *the energy functional* $L(\mathbf{y})$ *in* (26) *is wlsc in* $W^{2,2}(\Omega)$.

Proof. To prove this, we validate the three conditions of Lemma 3.7 as follows:

(i) First, the template image M and the moving image T are assumed to be continuously differentiable, their normalized gradients are hence continuous. It is easy to see that $f(\cdot)$ is a Carathéodory function.

(ii) Second, $f(\mathbf{x}, \mathbf{y}, \psi, \Theta)$ is convex with respect to Θ, so quasi-convex.

(iii) Finally, we have $|\nabla^*(M \circ \mathbf{y})| \leq 1$ and $|\nabla^* T| \leq 1$, which means

$$(|\nabla^*(M\circ\mathbf{y})|+|\nabla^*T|-|\nabla^*(M\circ\mathbf{y})+\nabla^*T|)^2 \leq (|\nabla^*(M\circ\mathbf{y})|+|\nabla^*T|)^2 \leq 4\,.$$

Given that $\Phi(v) = v^2/[(v-1)^2+1] \leq 2$ for any v, we have

$$\begin{aligned}
f(\mathbf{x}, \mathbf{y}, \psi, \Theta) &= \frac{\alpha_1}{2}|\psi - I|^2 + \frac{\alpha_2}{2}|\Theta|^2 + |\nabla^*(M \circ \mathbf{y}) - \nabla^* T|^2 \\
&+ (|\nabla^*(M \circ \mathbf{y})| + |\nabla^* T| - |\nabla^*(M \circ \mathbf{y}) + \nabla^* T|)^2 \\
&+ \beta\Phi(\frac{\|\psi\|_F^2 - n\,\mathrm{sign}_\epsilon(\det\psi)(\det\psi)^{2/n}}{\|\psi\|_F^2 + n\,\mathrm{sign}_\epsilon(\det\psi)(\det\psi)^{2/n}}) \\
&\leq \frac{\alpha_1}{2}|\psi|^2 + \frac{\alpha_2}{2}|\Theta|^2 + 2\beta + 2 + 4 \\
&\leq \frac{\alpha}{2}(|\mathbf{y}|^2 + |\psi|^2 + |\Theta|^2) + 2\beta + 6
\end{aligned}$$

where $\alpha = max\{\alpha_1, \alpha_2\}$. Then, the function $f(\cdot)$ satisfies $0 \leq f$ and $\leq a + C(|y|^2 + |\psi|^2 + |\Theta|^2)$; i.e., it fulfils condition (iii) of Lemma 4 with $a(x) \equiv a = 2\beta + 6$ and $C = \alpha/2$.

Hence, the function $f(\cdot)$ wlsc in $W^{2,2}(\Omega)$. □

Based on Lemma 1 and Lemma 2, we have the following result which proves the existence of a solution for the minimization model Eq.(22).

Theorem 3.9. *If T and M are continuously differentiable and compactly supported in Ω, then the minimization problem (22) with data fidelity (23) admits at least one solution in the space W, where $W = \{\mathbf{y} \in W^{2,2}(\Omega) : \mathbf{y}(\mathbf{x}) = \mathbf{x}$ on $\partial\Omega\}$.*

Proof. Since $L(\mathbf{y})$ has a lower bound 0, we can find a minimizing sequence $(\mathbf{y}_n)_{n\in N} \subset W$ of $L(\cdot)$, such that

$$L(\mathbf{y}_n) \underset{n\to\infty}{\to} m_1 := \underset{\mathbf{y}\in W}{inf}\, L(\mathbf{y}).$$

Using the positivity of $GF_{TM}(\mathbf{y})$ and the generalized Poincaré inequality, there exist constants $C_1, C_2 \in R$ such that

$$L(\mathbf{y}) \geq C_1\|\mathbf{y}\|^2_{W^{2,2}} + C_2.$$

Since $L(Id) = GF_{TM}(Id)$ is finite, we can assume that $(L(\mathbf{y}_n))n \in N$ is bounded by a constant $m_2 > 0$, which guarantees that the sequence $(\mathbf{y}_n)_{n\in N}$ is uniformly bounded in W:

$$m_2 \geq L(\mathbf{y}_n) \geq C_1 \|\mathbf{y}_n\|^2_{W^{2,2}} + C_2 \tag{27}$$

Since $W^{2,2}(\Omega)$ is a reflexive space, there exists a sub-sequence, denoted $(\mathbf{y}_{n_l})_{n_l\in N}$ such that $\mathbf{y}_{n_l} \underset{n\to\infty}{\to} \mathbf{y}*$ weakly in $W^{2,2}(\Omega)$. Applying the wlsc of the function $f(\cdot)$ in $W^{2,2}(\Omega)$ from Lemma 2, we have

$$\inf_{\mathbf{y}\in W} L(\mathbf{y}) = \lim_{n\to\infty} L(\mathbf{y}_n) = \lim_{n_l\to\infty} L(\mathbf{y}_{n_l}) \geq L(\mathbf{y}^*) \geq \inf_{\mathbf{y}\in W} L(\mathbf{y})$$

Hence, $\mathbf{y}^* \in W$. $\square$

In this work, let $\mathbf{u}(\mathbf{x})$ be the displacement field such that $\mathbf{y}(\mathbf{x}) := \mathbf{x}+\mathbf{u}(\mathbf{x})$. Then, the proposed optimization problem (22) can be equally reformulated in terms of $\mathbf{u}$ such that

$$\begin{aligned}\min_{\mathbf{u}} \tilde{L}(\mathbf{u})\big(= L(\mathbf{x}+\mathbf{u})\big) := D(M \circ (\mathbf{x}+\mathbf{u}), T) + \frac{\alpha_1}{2}\int_\Omega ||\nabla(\mathbf{u})||^2_F d\mathbf{x} \\ + \frac{\alpha_2}{2}\int_\Omega ||\nabla^2(\mathbf{u})||^2_F d\mathbf{x} + \beta \int_\Omega \Phi(\tilde{N}(\mathbf{u})) d\mathbf{x}\,,\end{aligned} \tag{28}$$

where **the penalty function** $\Phi(v) = v^2/[(v-1)^2+1]$ and the Beltrami coefficient-consistent measure $N(\mathbf{y})$ in (17) is represented identically as $\tilde{N}(\mathbf{u})$, w.r.t. $\mathbf{u}$, such that

$$\tilde{N}(\mathbf{u}) = N(\mathbf{x}+\mathbf{u}) = \frac{\|\mathbf{I}+\nabla\mathbf{u}\|^2_F - n\,\mathrm{sign}(\det(\mathbf{I}+\nabla\mathbf{u}))(\det(\mathbf{I}+\nabla\mathbf{u}))^{2/n}}{\|\mathbf{I}+\nabla\mathbf{u}\|^2_F + n\,\mathrm{sign}(\det(\mathbf{I}+\nabla\mathbf{u}))(\det(\mathbf{I}+\nabla\mathbf{u}))^{2/n}}\,, \tag{29}$$

and $\mathbf{I}$ is the identity matrix.

3.3. Numerical Implementations

In this section, we propose a coarse-to-fine incremental optimization strategy, see Fig. 1, to efficiently tackle the proposed challenging optimization problem (22) which is highly nonlinear and non-convex. The general framework of the introduced coarse-to-fine multi-level optimization solution can be illustrated as Alg. 1. Initially, two image pyramids are built upon the two given images of M and T from the coarsest image resolution level 1 to

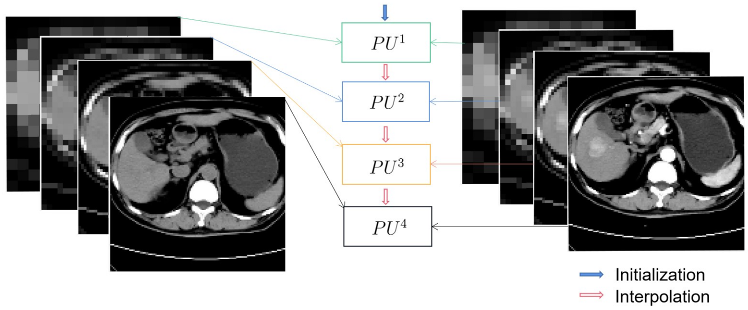

Figure 1: A coarse-to-fine incremental optimization scheme is applied to efficiently tackle the proposed optimization problem (22). This figure shows that, first, two image pyramids are built upon the two given images of M and T from the coarsest image resolution level 1 to the finest level L; the approximate solution at the coarser level $\ell - 1$ is taken as the starting value of $\mathbf{u}_0^\ell(\mathbf{x})$ at its next finer level ℓ, $\ell = 2...L$, so as to compute the incremental correction deformation field $\delta\mathbf{u}^\ell(\mathbf{x})$ iteratively (see (30)) for the corresponding optimization problem at each image resolution level.

the finest level L. The proposed coarse-to-fine algorithm starts from computing an initial approximation of the solution displacement field $\mathbf{u}(\mathbf{x})$ at the coarsest level $\ell = 1$, and the approximate solution at the coarser level $\ell - 1$ is interpolated and taken as the starting value of $\mathbf{u}_0^\ell(\mathbf{x})$ at its next finer level ℓ, $\ell = 1...L$, so as to resolve its incremental correction deformation field $\delta\mathbf{u}^\ell(\mathbf{x})$ iteratively (see (30)). In addition, **we follow the algorithm framework introduced in [29] and implement an efficient Gauss-Newton method to solve such incremental deformation field** $\delta\mathbf{u}(\mathbf{x})$ iteratively for the corresponding optimization problem at each image resolution level, see Alg. 2 for illustration, and a backtracking Armijo-line search to ensure a proper descent.

Now we show the necessary details of discretization and algorithm implementation in the following part. Let Y^ℓ denote the discretized transformation field at ℓ-th image resolution level, where $\ell = 1...L$, and U^ℓ the corresponding discretized displacement field. The initial value of U^ℓ is interpolated from the computed optimization result of $U^{\ell-1}$ at its previous coarser level $\ell - 1$. In addition, T^ℓ and M^ℓ represent the respective template and moving images at ℓ-th resolution level, computed by spline interpolation. We take a cell-centered discretization scheme in this work, where each element of the vector field U^ℓ is properly defined on the faces of each cell. The cell-centered transformation field Y^ℓ is hence given by

$$Y^\ell = X^\ell + PU^\ell$$

which is just the discretized version of $\mathbf{y}(\mathbf{x}) = \mathbf{x} + u(\mathbf{x})$ and P is an averaging operator mapping U^ℓ to its definition at each cell center.

Algorithm 1: Coarse-to-Fine Incremental Optimization Framework

Input: moving image M, template image T, the level of pyramid L.
Output: optimal transformation: $Y^L := X + PU^L$.

Initialize:
(1) built two image pyramids $\{M^l\}_{l=1}^L$ and $\{T^l\}_{l=1}^L$, respectively.
(2) set $U^0 = \mathbf{0}$ and $\delta u^0 = \mathbf{0}$;
while $1 \leq l \leq L$ **do**
  (1) $U^l = U^{l-1} + \delta u^{l-1}$ (including up-sampling).
  (2) $\delta u^l =$ **Algorithm 2**: Gauss-Newton(U^l);
  (3) $U^{l-1} = U^l$, $\delta u^{l-1} = \delta u^l$;
Finally, $U^L = U^{L-1} + \delta u^L$

In this context, the classical data-fidelity term (2) of sum squared differences (SSD) can be approximated as follows:

$$\frac{h}{2}\left(M^\ell(X^\ell + PU^\ell) - T^\ell\right)^T\left(M^\ell(X^\ell + PU^\ell) - T^\ell\right),$$

and, by simple computation, the data-fidelity term (23) of comparing normalized intensity gradients can be written as:

$$h\sum_{i=1}^{N}\left(8 - 4\sqrt{2 + 2\nabla_i M^\ell(X^\ell + PU^\ell)^T\nabla_i T^\ell}\right),$$

where ∇_i represents the discretized normalized gradient operator at cell i, $i = 1...N$.

On the other hand, the second and third terms of (28), which are the first and second-order regularizers, can be simply formulated as

$$\frac{h\alpha_1}{2}(U^\ell)^T A^T A U^\ell\,, \quad \frac{h\alpha_2}{2}(U^\ell)^T B^T B U^\ell\,,$$

where A and B are the discretized first and second-order derivative operators respectively.

For the new Beltrami coefficient-consistent term $\tilde{N}(\mathbf{u})$ defined in (29), it involves simple calculation of first-order derivatives and determinant. Let us denote $\tilde{N}^\ell(U^\ell)$ as its discrete version. In addition, we divide each cell in 3D into six tetrahedrons and assume that the displacement field is linear within each tetrahedron element. Thus, the last function term of (28) can be implemented as:

$$\sum_{i=1}^{N}\sum_{j=1}^{6}\frac{\beta h}{6}\Phi(\tilde{N}^\ell(U^\ell))\,.$$

Now we have the discretization implementation of each function term in (28) at ℓ-th image resolution level. Then, we can rewrite the whole energy function as $L^\ell(U^\ell)$. Since it is a unconstrained optimization problem, a search method is employed for optimizing it by the following iterative scheme:

$$U_{k+1}^\ell = U_k^\ell + \theta_k \delta U_k^\ell \tag{30}$$

where θ_k is the step-size obtained by an Armijo strategy and δU_k^ℓ is the search direction computed by Gauss-Newton method:

$$H_{U_k^\ell}\,\delta U_k^\ell \;=\; -\nabla_{U_k^\ell} L(U^\ell)\,, \tag{31}$$

where the matrix $H_{U_k^\ell}$ properly approximates the exact Hessian matrix $\nabla^2_{U_k^\ell} L(U^\ell)$ of $L^\ell(U^\ell)$ and $\nabla_{U_k^\ell} L(U_k^\ell)$ denotes the gradient of $L^\ell(U^\ell)$ at U_k^ℓ in Newton method. For example, by additional computation, the approximate gradient and Hessian matrix for our proposed optimization problem (28) with the sum-of-squared-differences (SSD) data term can be formulated as:

$$\begin{aligned}\nabla_{U_k^\ell} L(U_k^\ell) \;&= hP^T M_{U_k^\ell}^T (M^\ell(X^\ell + PU_k^\ell) - T^\ell)\\ &\quad + (h\alpha_1 A^T A + h\alpha_2 B^T B)U_k^\ell + \frac{\beta h}{6} d\vec{r}_{U_k^\ell}^{\,T} d\Phi_{\vec{r}}\end{aligned} \tag{32}$$

and

$$H_{U_k^\ell} = hP^T M_{U_k^\ell}^T M_{U_k^\ell} P + h\alpha_1 A^T A + h\alpha_2 B^T B + \frac{\beta h}{6} d\tilde{N}_{U_k^\ell}^T \mathrm{diag}(\Phi'')_{\tilde{N}}\, d\tilde{N}_{U_k^\ell} \tag{33}$$

Algorithm 2: Gauss-Newton Method

Input: moving image M^l, template image T^l, deformation field U^{l-1}
Output: incremental deformation field δu^l

Initialize:
(1) set the maximum number of iterations: K and stop conditions: S.
(2) set $\delta u_0^\ell = \mathbf{0}$; $U_0^l = U^{l-1} + u_0^\ell$;
(3) compute $H_{U_0^\ell}$ via Eq.(33), and $\nabla_{U_0^\ell} L(U_0^\ell)$ via Eq.(32)
while $1 \leq k \leq K$ *or not* S **do**
 (1) solve the linear equation Eq.(31) by MINRES solver to obtain δU_k^ℓ.
 (2) find θ_k by search method.
 (3) $\delta u_{k+1}^\ell = \delta u_k^\ell + \theta_k \delta U_k^\ell$.
 (4) compute $H_{\delta u_{k+1}^\ell}$ via Eq.(33), and $\nabla_{\delta u_{k+1}^\ell} L(\delta u_{k+1}^\ell)$ via Eq.(32)

where $M_{U_k^\ell} = \partial M^l(X^\ell + PU_k^\ell)/\partial U_k^l$ denotes the Jacobian of M^l with respect to U_k^l, $\mathrm{diag}(\Phi'')_{\tilde{N}}$ is a diagonal matrix with the diagonal elements $\Phi''(\tilde{N}_i)$, $i = 1, \cdots, 6N$.

Given that the matrices $hP^T M_{U_k^\ell}^T M_{U_k^\ell} P$ and $\frac{\beta h}{6} d\tilde{N}_{U_k^\ell}^T \mathrm{diag}(\Phi'')_{\tilde{N}}\, d\tilde{N}_{U_k^\ell}$ are semi-definite positive, and the matrix $h\alpha_1 A^T A + h\alpha_2 B^T B$ is positive definite, thus it is easy to verify that the approximate Hessian matrix $H_{U_k^\ell}$ is definite positive and a block matrix with low rank, which essentially guarantees (31) is solvable and simultaneously avoids a huge computational load for implementing the standard Newton method, especially for 3D medical image registration.

Particularly, a preconditioned MINRES solver is taken to solve the linear equation (31) efficiently, for which its preconditioner is composed of the diagonal elements of the matrix $H_{U_k^\ell}$. By ensuring the positive definiteness of the matrix $H_{U_k^\ell}$, the convergence of the proposed solver is confirmed.

4. Experiments

In this work, we conduct extensive experiments over both synthetic and real-world 3D medical images to show the effectiveness of the introduced Beltrami consistent image registration model (22) and the efficiency of the proposed optimization algorithm (as stated in Sec. 3.3) in numerics. Specifically, two experiments on registering images from the same image modality are studied in Sec. 4.1 (for 3D synthetic binary image registration) and Sec. 4.2 (for 3D brain MRI registration from the same MRI modality)[2]; three challenging 3D multi-modal image registration experiments are explored to align multiphase liver CT images in Sec. 4.3[3], CT-MRI liver images in Sec. 4.4[4] and brain MRIs from different subjects and imaging devices in Sec. 4.5.[5] In addition, the sum-of-squared-differences (SSD) is employed as the data fidelity measure for registering images from the same image modality and the normalized cross correlation (NCC) is explored as the data-fidelity metric for multi-modal image registration.

The following measurements are applied in our experiments to evaluate the performance of different approaches, in terms of accuracy and efficiency:

- Re_SSD is relative SSD between the fixed image T and the deformed image $M \circ \mathbf{y}$, given by $\|M \circ \mathbf{y} - T\|^2 / \|M - T\|^2$;

- DSC is the dice similarity coefficient evaluating the similarity of the segmented regions of interest, defined by $2|\Omega_M \circ \mathbf{y} \cap \Omega_T| / (|\Omega_M \circ \mathbf{y}| + |\Omega_T|)$ where $|\cdot|$ represents the total number of voxels in the specified region;

- $\min \det \nabla$ and $\max \det \nabla$ denote the minimum and maximum of the Jacobian determinant of the computed transformation field $\mathbf{y}$ respectively;

- TRE is the target registration error defined by $\sum_{i=1}^{n} dist(\mathbf{x}_i, \mathbf{y}(\mathbf{x}_i))/n$, where $\mathbf{x}_i$ and $\mathbf{y}(\mathbf{x}_i)$ represent the corresponding landmarks in two images, n is the number of landmarks and $dist(\cdot)$ gives the distance between two landmarks;

- Iter represents the total number of iterations to reach convergence.

For comparisons, all the experiments are set up and performed on the same laptop with Windows 10, Intel core i7-9750H CPU @2.60 GHz and

[2]The 3D brain MR images are from the open software package FAIR [3].

[3]The 3D multiphase liver CT images are provided by the First Affiliated Hospital, College of Medicine, Zhejiang University, China.

[4]The images for 3D liver CT-MRI image registration are also provided by the First Affiliated Hospital, College of Medicine, Zhejiang University, China.

[5]The 39 image pairs for 3D multi-modal MRI brain images in Sec. 4.5 are taken from the open data sets given in [30].

16GB memory; our proposed approach and five state-of-the-art methods including the ones based on ZC (11), ZCO1 (9), ZCO2 (10), Hyper ([7]) and LDDMM ([6]), are implemented and explored in Matlab 2019a, where the recently proposed approaches of ZC, ZCO1 and ZCO2 are in the same category of Beltrami coefficient-related methods as our proposed Beltrami coefficient-consistent method in this study.

4.1. Experiments on Synthetic Image Registration

Table 1: Parameter settings for synthetic image registration

Method	α_1	α_2	β
Ours	100	0.1	1500
ZC	100	0.1	6200
ZCO1	100	0.1	2000
ZCO2	100	0.1	50
Hyper	$\alpha_l = 100$	$\alpha_s = 1$	$\alpha_v = 10$
LDDMM	$\alpha = 1200$	$Nt = 10$	

We first conduct experiments on registering two 3D synthetic images through our proposed method and five state-of-the-art methods of ZC, ZCO1, ZCO2, Hyper and LDDMM for comparisons. Detailed parameter settings for each approach are shown in Tab. 1. Experiment results are demonstrated graphically in Fig. 2. It is obvious that the results obtained by the Beltrami-coefficient-related approaches, i.e. ours, ZC, ZCO1 and ZCO2, are better than the other two methods of Hyper and LDDMM; especially, in view of the local relative volume change $\det \nabla \mathbf{y}$, the computed transformation field $\mathbf{y}(\mathbf{x})$ by our proposed method is more reasonable than the ones computed by ZC, ZCO1 and ZCO2. Moreover, as shown in Tab. 2, our proposed approach performed the best in terms of DSC, and slightly worse than ZC in Re_SSD. In fact, the actual Re_SSD by our method is $8.57e-04$ comparing with $8.37e-04$ achieved by ZC, which are nearly the same but better than the other approaches. By the result ($\min \det \nabla$) given in Tab. 2, which presents the minimum of the Jacobian determinant of the computed transformation field, all the values are positive such that all the result transformation fields are topology-preserving. Especially, by the difference between $\min \det \nabla$ and $\max \det \nabla$ given in Tab. 2, which corresponds to the range of relative volume change ($\det \nabla \mathbf{y}$), one can easily see that the method of Hyper got the least value, which is due to its unreasonable enforcement of $\det \nabla \mathbf{y}$ to be one; in contrast, the other approaches obtained similar bigger ranges of $\det \nabla \mathbf{y}$. Also, the Beltrami-coefficient-related methods of ours, ZC, ZCO1 and ZCO2 are more efficient than the other two methods of Hyper and LDDMM, in terms of computation time and total iteration numbers.

Table 2: Comparisons of synthetic image registration

	DSC	Re_SSD(%)	$\min\det\nabla$	$\max\det\nabla$	time(s)	Iter
Ours	0.927	**0.09**	0.36	38.99	17	[8,4,3,4]
ZC	0.924	**0.08**	0.36	36.84	15	[13,5,3,4]
ZCO1	0.921	**0.11**	0.35	37.80	16	[10,4,3,4]
ZCO2	0.923	**0.12**	0.35	35.48	14	[11,4,3,4]
Hyper	0.875	**1.26**	0.12	16.47	55	[20,6,6,7]
LDDMM	0.872	**1.31**	0	38.10	798	[4,2,2,2]

4.2. Experiments on 3D Brain MRI Registration

Table 3: Parameter settings for 3D brain MRI registration

Method	α_1	α_2	β
Ours	100	0.1	4000
ZC	100	0.1	5000
ZCO1	100	0.1	5000
ZCO2	100	0.1	70
Hyper	$\alpha_l = 100$	$\alpha_s = 10$	$\alpha_v = 100$
LDDMM	$\alpha = 200$	$Nt = 2$	

The experiments on registering two 3D images from the same brain MRI modality are conducted to show the performance of mono-modal image registration by all the compared algorithms. The two images are from the open data sets in the software of FAIR [3]. Detailed parameter settings of each experiment are shown in Tab.3, where the Hyper's are provided by FAIR. Experiment results are visually shown in Fig. 3, and their key measurements are given in Tab. 4 for evaluation. As we can see, the minimums of Jacobian determinant of the obtained results are positive such that all the methods properly achieved the topology-preserving transformation results as the results. In addition, our proposed approach performed the best in DSC, but

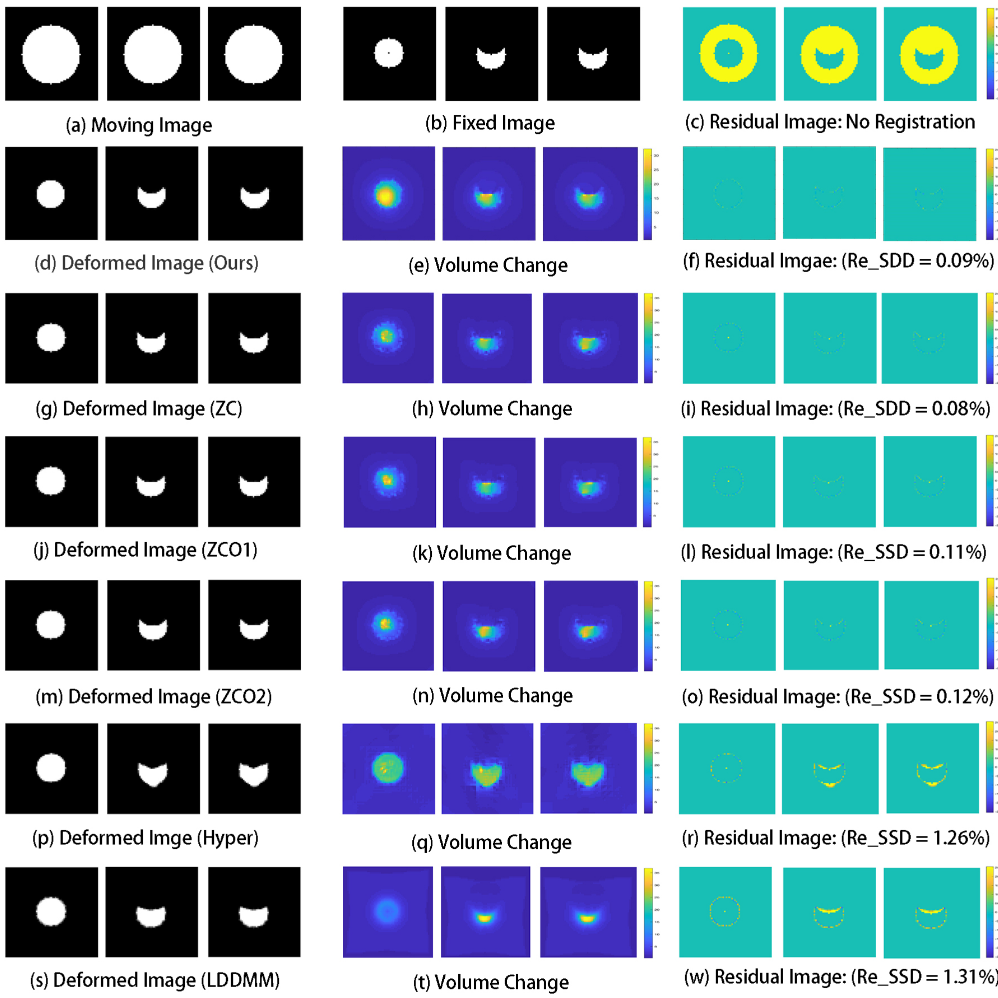

Figure 2: This figure visually illustrates the experiment results on registering two 3D synthetic images through different approaches for comparisons: the first row shows the moving image $M(\mathbf{x})$ to be registered, the template (fixed) image $T(\mathbf{x})$ and the residual image before registration in axial, coronal, and sagittal views. The experiment results by the approaches of ours, ZC, ZCO1, ZCO2, Hyper and LDDMM are shown from the second row to the seventh row respectively. At each row, the deformed image by the computed transformation $\mathbf{y}$, its corresponding relative volume change $(\det \nabla \mathbf{y})$ and residual image of Re_SSD in axial, coronal, and sagittal views. The percentage represents the relative residual.

slightly worse than ZC in Re-SSD. Still, by the difference between $\min \det \nabla$ and $\max \det \nabla$ given in Tab. 4, the method of Hyper clearly got the least range of relative volume change, due to its strong enforcement of $\det \nabla \mathbf{y}$ to be one; in contrast, the range of relative volume change obtained by our approach is more reasonable than the other approaches. For numerical performance, the he Beltrami-coefficient-related methods of ours, ZC, ZCO1 and ZCO2 performed more efficient than the other two methods of Hyper and LDDMM, with much less computation time.

Table 4: Comparisons of 3D brain MRI registration

	DSC	Re_SSD(%)	$\min \det \nabla$	$\max \det \nabla$	time(s)	Iter
Ours	0.893	**9.77**	0.16	19.62	243	[8,11,11,13]
ZC	0.863	**8.12**	0.01	39.36	296	[9,11,13,16]
ZCO1	0.855	**11.93**	0.05	36.64	189	[7,11,13,10]
ZCO2	0.858	**9.95**	0.06	43.91	222	[5,9,11,14]
Hyper	0.856	**11.33**	0	4.64	581	[8,9,16,24]
LDDMM	0.842	**18.59**	0	17.89	774	[3,5,7,8]

4.3. Experiments on Multi-Phase CT Image Registration

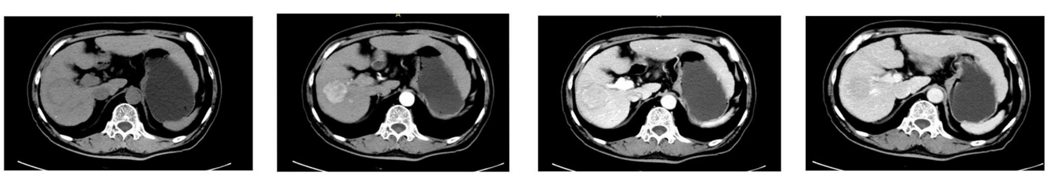

(a) Pre-Constrast Phase (b) Arterial Phase (c) Portal Venous Phase (d) Delayed Phase

Figure 4: Acquired CT images of four different imaging phases.

In this part, we explore experiments on registering 3D multi-phase CT images which are acquired during different imaging phases (see Fig. 4 for illustration). As shown in Fig. 4, breathing and other physiological motions during imaging cause misalignment between CT images acquired at different imaging phases. Obviously, the often-used sum of squared differences (SSD) is inappropriate as the data fidelity measure for registering such multi-phase CT images, due to the lack of intensity consistency between corresponding

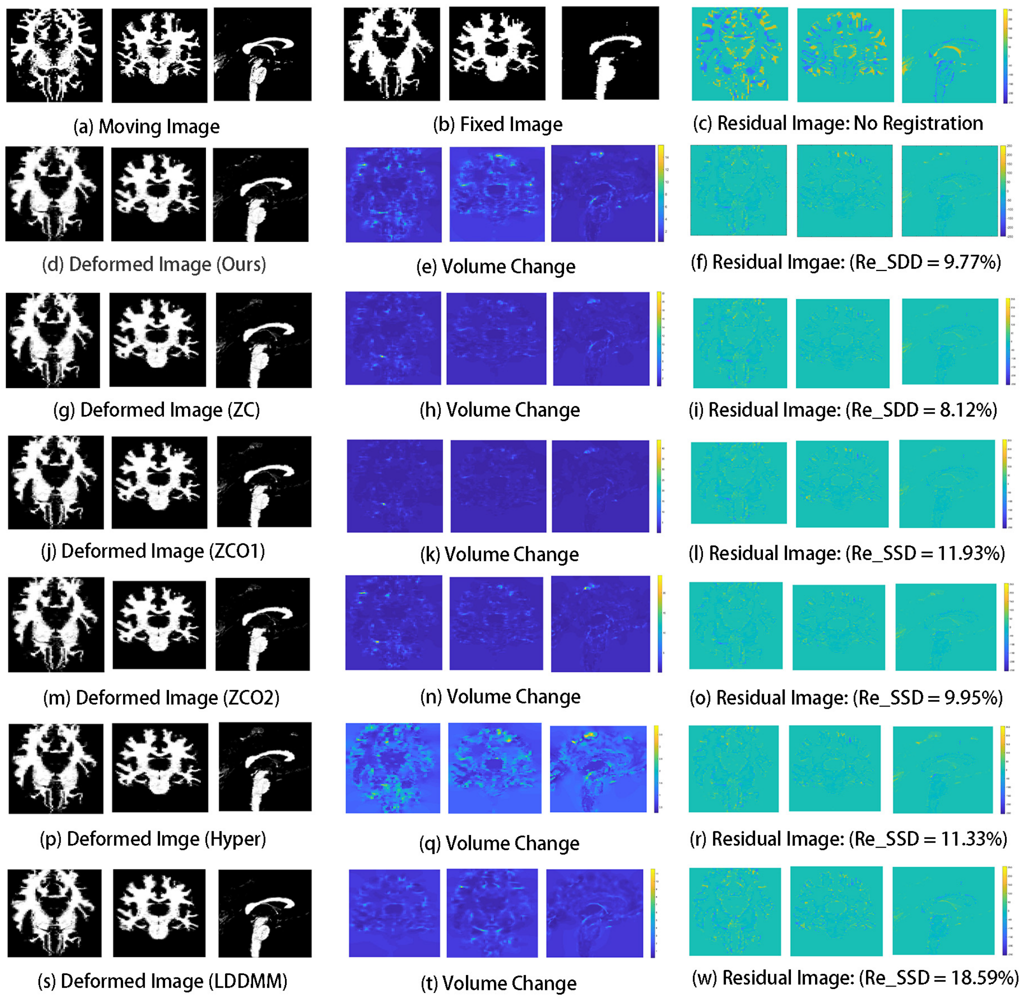

Figure 3: This figure visually illustrates the experiment results on registering two 3D brain images through different approaches for comparisons: the first row shows the moving image $M(\mathbf{x})$ to be registered, the template (fixed) image $T(\mathbf{x})$ and the residual image before registration in axial, coronal, and sagittal views. The experiment results by the approaches of ours, ZC, ZCO1, ZCO2, Hyper and LDDMM are shown from the second row to the seventh row respectively. At each row, the deformed image by the computed transformation $\mathbf{y}$, its corresponding relative volume change ($\det \nabla \mathbf{y}$) and residual image of Re_SSD in axial, coronal, and sagittal views, where the percentage represents the relative residual (Re_SSD).

image pixels at different imaging phases. The normalized cross correlation (NCC) is employed to reliably evaluate differences between CT images acquired at different phases. During this experiment, comparing normalized intensity gradients is thus utilized as the data fidelity measure, see (23); and the similarity between the segmented liver regions in the fixed image and deformed moving image is evaluated as DSC.

Table 5: Parameter settings for multi-phase CT image registration

Method	α_1	α_2	β
Ours	0.1	0.01	0.1
ZC	0.1	0.01	0.1
ZCO1	0.1	0.01	0.01
ZCO2	0.1	0.01	0.3

Detailed parameter settings, for our proposed approach and three other state-of-the-art methods of ZC, ZCO1, ZCO2 are shown in Tab. 5. Five 3D multi-phase CT image series are used for experiments, where, for each image series, we take the arterial phase image as the fixed image and the pre-contrast and delayed images as the corresponding moving images. Hence, 10 image registration experiments in total are performed and the experiment results are summarized in Tab. 6 in the form of mean ± std. It is obvious to see that our proposed method obtained the best accuracy results in terms of DSC and TRE, which are better than the other Beltrami-coefficient-related approaches; also, ZCO2 got results slightly worse than our proposed approach in accuracy, but performed much slower than ours. In general, as Tab. 6, the Beltrami-coefficient-related methods of ours, ZC, ZCO1 and ZCO2 performed similarly in terms of computation time. By the obtained results of ($\min \det \nabla$), all the values are above zero such that the result transformation fields are topology-preserving.

Table 6: Comparisons of multi-phase CT image registration

	DSC	TRE(mm)	$\min \det \nabla$	$\max \det \nabla$	Time (s)
Ours	0.955 ± 0.011	4.10 ± 1.57	0.13 ± 0.03	2.67 ± 0.25	246 ± 54
ZC	0.955 ± 0.011	4.21 ± 1.50	0.06 ± 0.03	2.86 ± 0.53	422 ± 133
ZCO1	0.950 ± 0.014	4.49 ± 1.41	0.30 ± 0.07	2.05 ± 0.18	89 ± 53
ZCO2	0.956 ± 0.011	4.14 ± 1.30	0.13 ± 0.05	3.08 ± 0.46	337 ± 80

4.4. Experiments on CT-MRI Image Registration

In this experiment, six pairs of 3D CT (portal venous phase) and T_1 enhanced MRI images, from six different subjects who were pathologically proven belong to intrahepatic cholangiocarcinoma (ICC), are applied for CT-MRI registration. For each image pair, we fix the CT image as the template image and the T_1 enhanced MRI image as the moving image. The normalized cross correlation (NCC) is used as the data-fidelity metric for the challenging CT-MRI registration task, given the totally different image modalities of CT and MRI. Detailed parameter settings for our proposed approach and three other state-of-the-art methods of ZC, ZCO1, ZCO2 are given in Tab. 7, and experiment results are summarized in Tab. 8.

Table 7: Parameter settings for CT-MRI image registration

Method	α_1	α_2	β
Ours	0.01	0.01	0.3
ZC	0.01	0.01	1
ZCO1	0.01	0.01	**0.0001**
ZCO2	0.01	0.01	0.1

Table 8: Comparisons of CT-MRI image registration

	DSC	NCC	min det ∇	max det ∇	Time (s)
Ours	0.900 ± 0.030	0.737 ± 0.027	0.17 ± 0.03	3.50 ± 0.40	178 ± 40
ZC	0.899 ± 0.029	0.732 ± 0.052	0.11 ± 0.02	3.43 ± 0.31	175 ± 46
ZCO1	0.891 ± 0.029	0.698 ± 0.047	0.02 ± 0.01	2.25 ± 0.30	86 ± 8
ZCO2	0.898 ± 0.029	0.734 ± 0.050	0.12 ± 0.03	3.46 ± 0.54	135 ± 22

The similarity between the segmented liver regions in the fixed image and deformed moving image is use for DSC computation during this experiment. As shown in Tab. 8, our proposed method outperforms the other approaches in registration accuracy, i.e. DSC and NCC. All the computed transformation fields are topology-preserving with positive Jacobian determinants. By computation time given in Tab. 8, it is obvious to see that all the Beltrami-coefficient-related approaches of ours, ZC, ZCO1 and ZCO2 achive similar efficiency in numeric.

4.5. Experiments on Brain MRI Registration

In this work, 40 3D brain MRIs from different subjects are used for image registration experiments. We fix the first image as the template image and the other ones as the moving images. 39 image pairs are hence made for experiments. Moreover, both fixed and moving images are in the same image modality, so the normalized cross correlation (NCC) can also work as a reliable data fidelity measure in the experiments. Detailed parameter settings for our proposed approach and three other state-of-the-art methods of ZC, ZCO1, ZCO2 are given in Tab. 9, and experiment results are summarized in Tab. 10.

Table 9: Parameter settings for brain MRI registration

Method	α_1	α_2	β
Ours	0.1	6	20
ZC	0.1	6	3
ZCO1	0.1	20	0.1
ZCO2	0.1	6	15

In this experiment, the similarity of 56 segmented brain regions between the fixed image and deformed moving image is evaluated in DSC. As shown in Tab. 10, all DSC values are not high cause not all the segmented brain regions are exactly correct. Still, in view of DSC and NCC, i.e. accuracy, our proposed method achieves the best result. Generally, all the Beltrami-coefficient-related approaches of ours, ZC, ZCO1 and ZCO2 perform similar in computational efficiency. Given the positive results of ($\min \det \nabla$), all the result transformation fields are thus topology-preserving.

Table 10: Comparisons of brain MRI registration

	DSC	NCC	$\min \det \nabla$	$\max \det \nabla$	Time (s)
Ours	0.687 ± 0.011	0.981 ± 0.002	0.35 ± 0.04	2.59 ± 0.20	352 ± 46
ZC	0.683 ± 0.012	0.982 ± 0.002	0.11 ± 0.03	3.19 ± 0.29	420 ± 57
ZCO1	0.681 ± 0.012	0.975 ± 0.002	0.26 ± 0.07	2.20 ± 0.15	312 ± 34
ZCO2	0.686 ± 0.012	0.981 ± 0.002	0.33 ± 0.03	2.68 ± 0.22	336 ± 47

5. Discussions

Multiple dimensional Beltrami-like measures, see their 3D cases (9)-(11) for example, were introduced and studied in recent studies [19, 20]. Particularly, as shown in (16), the nD Beltrami-like measure $N(\mathbf{y})$ (14) is related but is not equivalent to the standard Beltrami coefficient in 2D. They are, however, not exactly the same in 2D. In another word, the generalized nD Beltrami-like measure $N(\mathbf{f})$ given in (14) does not results in the original 2D Beltrami coefficient while $n = 2$, i.e. not consistent with the original 2D Beltrami coefficient. In addition, such Beltrami-like measure (14) in nD may explicitly require $\det \nabla\mathbf{y} > 0$ due to the parity of n. In contrast, as opposed to the Beltrami-like measure (14), the proposed novel nD Beltrami measure (17) does not need considering the parity of n since the sign of $\det \nabla\mathbf{f}$ is built-in; also, for the 2D case ($n = 2$), the new measure (17) precisely boils down to the standard Beltrami coefficient, which is consistent with the definition of 2D Beltrami coefficient. In addition, the proposed Beltrami measure (17) holds the properties (Lemma 3.2) in nD and satisfies Coro. 3.3, Prop. 3.4 - 3.5, which means that it can be seen as a natural extension of the classical Beltrami coefficient.

On the other hand, as demonstrated in Sec. 4, the regularization function of the proposed new Beltrami-consistent measure performs more reliably, in terms of accuracy, distortion justification and efficiency, than the other Beltrami-like measures and two other often-used methods of LDDMM and Hyper in experiments of topology-preserving image registration. In most experiments, the approach based on the proposed Beltrami-consistent measure achieved the best in the accuracy of aligning regions of interest (ROI), and nearly the best in matching gray-values or image features pixel-wise in terms of Re_SSD, while obtaining convergence with similar efficiency as the other Beltram-like based approaches of ZC1, ZCO1 and ZCO2, but faster than the two methods of Hyper and LDDMM, see the corresponding table of each experiment in Sec. 4 for comparisons. In addition, by the difference between $\min\det\nabla$ and $\max\det\nabla$ shown in the experiment results, it is clear that the proposed approach often results in a deformation field with reasonable gap between $\min\det\nabla$ and $\max\det\nabla$, comparing to the often over-smoothed results generated by the methods of Hyper and LDDMM with a much smaller gap between $\min\det\nabla$ and $\max\det\nabla$. For example, for experiments of 3D brain MRI registration conducted in Sec. 4.2, the proposed approach based the introduced Beltrami-consistent measure achieved the most accurate result in terms of both DSC and Re_SSD, while obtaining the result deformation field with a reasonable difference of $\min \det \nabla$ and $\max \det \nabla$ (about 19, cf. over 35 for the other Beltrami-based methods and 4 for LDDMM); meanwhile, the computational efficiency of the four Beltrami-based methods, i.e. ours, ZC, ZCO1 and ZCO2, are mostly similar (around 200 sec.), but still much better than the other two approaches of Hyper and LDDMM (about 600 sec. - 700 sec.).

During the modern decade of deep learning renaissance, researchers have shown a rapidly increased interest in deep learning based image registration [31], especially non-rigid image registration [32, 33], which allows an excellent performance in computational efficiency. However, few of them [34, 35] were developed to enforce a diffeomorphic result. However, topology-preservation is not well kept in practice and grid folding is still often observed in results, see Tab. 11. We trained the framework of Voxelmorph [34] over image datasets of ADNI [36], ABIDE [37] and ADHD [38], using default parameters and two **batchsize** of 1 and 4 (Voxelmorph1 and Voxelmorph4). The result network of Voxmorph was evaluated on the same experiments of brain MRI registration in Sec. 4.5. We list the same results obtained in Sec. 4.5 for contrast. Obviously, as shown in Tab. 11, both deep learning-based methods of Voxelmorph1 and Voxelmorph4 obtained the worst results in DSC. Especially, both deep learning-based methods failed to preserving topology, observing that the smallest Jacobi determinant ($\min \det \nabla$) of the result mapping is obtained less than 0, i.e. grid folding, for some experiments.

Table 11: Comparisons with deep learning-based methods

	DSC	NCC	$\min \det \nabla$	$\max \det \nabla$	Time (s)
Ours	0.687 ± 0.011	0.981 ± 0.002	0.35 ± 0.04	2.59 ± 0.20	352 ± 46
ZC	0.683 ± 0.012	0.982 ± 0.002	0.11 ± 0.03	3.19 ± 0.29	420 ± 57
ZCO1	0.681 ± 0.012	0.975 ± 0.002	0.26 ± 0.07	2.20 ± 0.15	312 ± 34
ZCO2	0.686 ± 0.012	0.981 ± 0.002	0.33 ± 0.03	2.68 ± 0.22	336 ± 47
Hyper	0.663 ± 0.013	0.961 ± 0.005	0.70 ± 0.04	1.19 ± 0.04	11131 ± 2184
LDDMM	0.657 ± 0.015	0.941 ± 0.005	0.19 ± 0.10	1.89 ± 0.08	3834 ± 951
Voxelmorph4	$\mathbf{0.516 \pm 0.074}$	0.979 ± 0.003	$\mathbf{-0.01 \pm 0.16}$	11.17 ± 3.56	2.75 ± 0.10
Voxelmorph1	$\mathbf{0.515 \pm 0.071}$	0.979 ± 0.003	$\mathbf{0.03 \pm 0.03}$	11.29 ± 4.15	2.61 ± 0.12

6. Conclusions

In this paper, we develop a novel measure for evaluating local distortion of an nD diffeomorohic mapping, which gives rise to **the classical Beltrami coefficient in 2D**; namely, the new nD distortion measure is consistent with the original definition of Beltrami coefficient in 2D. This is missing in previous literature, but of great interest in quantifying local distortions of an nD quasi-conformal mapping and regularizing such mapping in the challenging topology-preserving image registration tasks. We further show its key mathematical properties, and introduce a new variational model for nD topology-preserving image registration by regularizing the proposed Beltrami-consistent coefficient. Experiments over different topology-preserving medical image registration tasks exactly show that the proposed Beltrami-consistent coefficient-based approach outperforms the other state-of-the-art topology-preserving image registration methods in both efficiency and accuracy. For the proposed optimization model, **the applied smooth penalty function works well to enforce the introduced Beltrami-consistent coefficient less than one, i.e. the constraint on topology preservation holds (see Lemma 3.2), when it is small enough in practice.** However, it is still of interest to study the penalty function alternatives **to make the topology preserving constraint strictly hold, for example a logarithmic barrier function,** even though this may increase computational complexities in numeric. Some other interesting studies, such as the proposed image registration model incorporating with a volume-preserving prior to improve robustness and accuracy of image registration etc., will appear in our future works. In addition, implementing the exact topology-preservation constraint and the proposed Beltrami-consistent coefficient-based regularization for diffeomorphic image registration over a modern deep learning framework is still open but of great interest in practice.

7. Author Contributions

The first two authors (Chongfei Huang and Ke Chen) have equal contributions, and the corresponding author is Jing Yuan (email: jyuan@zjnu.edu.cn). We list the contribution of each author as follows: theory and methodology: Chongfei Huang, Ke Chen and Jing Yuan; writing and revision: Chongfei Huang and Jing Yuan; implementation and experiment validation: Chongfei

Huang and Ke Chen; data organization and preprocessing: Chongfei Huang, Ke Chen, Dexing Kong and Meixiang Huang. All authors have read and agreed to the published version of the manuscript.

8. Acknowledgments

This work was supported by the National Natural Science Foundation of China (Grant No. 61877047, Grant No.12126607).

References

[1] A. Sotiras, C. Davatzikos, N. Paragios, Deformable medical image registration: A survey, IEEE Transactions on Medical Imaging 32 (7) (2013) 1153–1190. doi:10.1109/TMI.2013.2265603.

[2] K. Chen, L. M. Lui, J. Modersitzki, Image and surface registration, in: Processing, Analyzing and Learning of Images, Shapes, and Forms: Part 2, 2019, pp. 579–611. doi:https://doi.org/10.1016/bs.hna.2019.07.001.

[3] J. Modersitzki, FAIR: flexible algorithms for image registration, SIAM, 2009.

[4] J. Modersitzki, Numerical methods for image registration, Oxford University Press, 2003. doi:10.1093/acprof:oso/9780198528418.001.0001.

[5] A. Theljani, K. Chen, An augmented Lagrangian methods for solving a new variational model based on gradients similarity measures and high order regulariation for multimodality registration, Inverse Problems and Imaging 13 (2) (2019) 309–335. doi:10.3934/ipi.2019016.

[6] M. F. Beg, M. Miller, A. Trouvé, L. Younes, Computing large deformation metric mappings via geodesic flows of diffeomorphisms, International Journal of Computer Vision 61 (2) (2005) 139–157. doi:10.1023/B:VISI.0000043755.93987.aa.

[7] M. Droske, M. Rumpf, A variational approach to nonrigid morphological image registration, SIAM Journal on Applied Mathematics 64 (2) (2004) 668–687. doi:10.1137/S0036139902419528.

[8] H. Han, Z. Wang, A diffeomorphic image registration model with fractional-order regularization and Cauchy-Riemann constraint, SIAM Journal on Imaging Sciences 13 (3) (2020) 1240–1271. doi:10.1137/19M1260621.

[9] E. Haber, J. Modersitzki, Intensity gradient based registration and fusion of multi-modal images, in: Methods of Information in Medicine, 2006, pp. 726–733. doi:10.1007/11866763_89.

[10] F. Maes, A. Collignon, D. Vandermeulen, G. Marchal, P. Suetens, Multimodality image registration by maximization of mutual information, IEEE Transactions on Medical Imaging 16 (2) (1997) 187–198. doi:10.1109/42.563664.

[11] C. Broit, Optimal registration of deformed images, University of Pennsylvania, 1981.

[12] G. Christensen, R. Rabbitt, M. Miller, Deformable templates using large deformation kinematics, IEEE Transactions on Image Processing 5 (10) (1996) 1435–1447. doi:10.1109/83.536892.

[13] B. Fischer, J. Modersitzki, Fast diffusion registration, Contemporary Mathematics 313 (2002) 117–128.

[14] C. Frohn-Schauf, S. Henn, K. Witsch, Multigrid based total variation image registration, Computing and Visualization in Science 11 (2) (2008) 101–113. doi:10.1007/s00791-007-0060-2.

[15] B. Fischer, J. Modersitzki, Curvature based image registration, Journal of Mathematical Imaging and Vision 18 (1) (2003) 81–85. doi:10.1023/A:1021897212261.

[16] B. Fischer, J. Modersitzki, A unified approach to fast image registration and a new curvature based registration technique, Linear Algebra and its Applications 380 (2004) 107–124.

[17] J. Zhang, K. Chen, Variational image registration by a total fractional-order variation model, Journal of Computational Physics 293 (2015) 442–461.

[18] L. K. Chun, L. M. Lui, Landmark and intensity based registration with large deformations via quasi-conformal maps, SIAM Journal on Imaging Sciences 7 (4) (2013). doi:10.1137/130943406.

[19] D. Zhang, K. Chen, 3D orientation-preserving variational models for accurate image registration, SIAM Journal on Imaging Sciences 13 (3) (2020) 1653–1691. doi:10.1137/20M1320006.

[20] Y. T. Lee, K. C. Lam, L. M. Lui, Landmark-matching transformation with large deformation via n-dimensional quasi-conformal maps, Journal of Scientific Computing 67 (3) (2016) 926–954. doi:10.1007/s10915-015-0113-5.

[21] H.-L. Chan, S. Yan, L.-M. Lui, X.-C. Tai, Topology-preserving image segmentation by Beltrami representation of shapes, Journal of Mathematical Imaging and Vision 60 (2018) 401–421.

[22] D. Zhang, X.-C. Tai, L. M. Lui, Topology- and convexity-preserving image segmentation based on image registration, Applied Mathematical Modelling 100 (2021) 218–239.

[23] A. Trouve, Diffeomorphisms groups and pattern matching in image analysis, International Journal of Computer Vision 28 (3) (1998) 213–221. doi:10.1023/A:1008001603737.

[24] L. Ruthotto, Hyperelastic image registration - theory, numerical methods, and applications, Ph.D. thesis, University of Lübeck (2012).

[25] M. Burger, J. Modersitzki, L. Ruthotto, A hyperelastic regularization energy for image registration, SIAM Journal on Scientific Computing 35 (1) (2013) B132–B148. doi:10.1137/110835955.

[26] A. Mang, L. Ruthotto, A Lagrangian Gauss-Newton-Krylov solver for mass- and intensity-preserving diffeomorphic image registration, SIAM Journal on Scientific Computing 39 (5) (2017) B860–B885. doi:10.1137/17M1114132.

[27] T. Iwaniec, G. Martin, Geometric function theory and non-linear analysis, Clarendon Press, 2001.

[28] X. Zhou, Weak lower semicontinuity of a functional with any order, Journal of Mathematical Analysis and Applications 221 (1) (1998) 217–237. doi:10.1006/jmaa.1997.5881.

[29] D. Zhang, A. Theljani, K. Chen, On a new diffeomorphic multi-modality image registration model and its convergent Gauss-Newton solver, Journal of Mathematical Research with Applications 39 (6) (2019) 633–656.

[30] D. W. Shattuck, M. Mirza, V. Adisetiyo, C. Hojatkashani, G. Salamon, K. L. Narr, R. A. Poldrack, R. M. Bilder, A. W. Toga, Construction of a 3D probabilistic atlas of human cortical structures, Neuroimage 39 (3) (2008) 1064–1080.

[31] G. Haskins, U. Kruger, P. Yan, Deep learning in medical image registration: a survey, Machine Vision and Applications 31 (2020) 1–18.

[32] G. Balakrishnan, A. Zhao, M. R. Sabuncu, J. Guttag, A. V. Dalca, An unsupervised learning model for deformable medical image registration, in: Proceedings of the IEEE conference on computer vision and pattern recognition (CVPR), 2018, pp. 9252–9260.

[33] Z. Zheng, W. Cao, Y. Duan, G. Cao, D. Lian, Multi-strategy mutual learning network for deformable medical image registration, Neurocomputing 501 (2022) 102–112.

[34] G. Balakrishnan, A. Zhao, M. R. Sabuncu, J. Guttag, A. V. Dalca, Voxelmorph: A learning framework for deformable medical image registration, IEEE Transactions on Medical Imaging 38 (8) (2019) 1788–1800.

[35] B. Kim, D. H. Kim, S. H. Park, J. Kim, J.-G. Lee, J. C. Ye, Cyclemorph: cycle consistent unsupervised deformable image registration, Medical Image Analysis 71 (2021) 102036.

[36] S. G. Mueller, M. W. Weiner, L. J. Thal, R. C. Petersen, C. R. Jack, W. Jagust, J. Q. Trojanowski, A. W. Toga, L. Beckett, Ways toward an early diagnosis in Alzheimer's disease: the Alzheimer's Disease Neuroimaging Initiative (ADNI), Alzheimer's and Dementia 1 (1) (2005) 55–66.

[37] A. Di Martino, C.-G. Yan, Q. Li, E. Denio, F. X. Castellanos, K. Alaerts, J. S. Anderson, M. Assaf, S. Y. Bookheimer, M. Dapretto, et al., The

autism brain imaging data exchange: towards a large-scale evaluation of the intrinsic brain architecture in autism, Molecular Psychiatry 19 (6) (2014) 659–667.

[38] P. Bellec, C. Chu, F. Chouinard-Decorte, Y. Benhajali, D. S. Margulies, R. C. Craddock, The neuro bureau ADHD-200 preprocessed repository, Neuroimage 144 (2017) 275–286.